nature communications

Article

https://doi.org/10.1038/s41467-025-57889-1

Three-dimensional flexible thermoelectric fabrics for smart wearables

Received: 2 October 2024

Accepted: 4 March 2025

Published online: 14 March 2025

Check for updates

Xinyang He[1,5], Xiao-Lei Shi[2,5], Xiaoyun Wu[2], Chengzu Li[1], Wen-Di Liu[1], Honghua Zhang[3], Xuliang Yu[4], Liming Wang[1] ✉, Xiaohong Qin[1] ✉ & Zhi-Gang Chen[2] ✉

Wearable thermoelectric devices, capable of converting body heat into electrical energy, provide the potential driving power for the Internet of Things, artificial intelligence, and soft robotics. However, critical parameters have long been overlooked for these practical applications. Here, we report a three-dimensional flexible thermoelectric device with a structure featuring an inner rigid and outer flexible woven design. Such a structure includes numerous small static air pockets that create a stable out-of-plane temperature difference, enabling precise temperature signal detection (accuracy up to 0.02 K). Particularly, this structure exhibits excellent multi-signal decoupling capability, excellent elasticity (>10,000 compression cycles), ultra-fast compression response (20 ms), stable output signal under 50% compressive strain, high breathability (1300 mm s^{-1}), and washability. All these metrics achieve the highest values currently reported, fully meeting the requirements for body heat and moisture exchange, as demonstrated in our designed integrated smart mask and smart glove systems based on vector machine learning technology. This work shows that our three-dimensional flexible thermoelectric device has broad applicability in wearable electronics.

The rapid development of the Internet of Things (IoT), artificial intelligence (AI), and soft robotics has driven the demand for flexible electronic devices[1–5]. These devices enable energy harvesting and stimuli detection in both humans and environments and can serve as the ultimate platform for data collection and transmission in human-machine interaction (HMI)[6–8]. Among these, wearable electronic systems that offer comfort, high integration, and portability are considered potential candidates for the next generation of smart wearable devices[4,9,10]. Through thoughtful structural design and molecular engineering modifications, these systems can be enhanced with advanced functionalities, including energy harvesting, thermo-hygro regulation, and multi-stimuli transmission. Among the various functional wearable electronics, wearable flexible thermoelectric devices (F-TEDs) stand out as excellent candidates for wearable energy harvesting and conversion systems[11–18]. These devices directly convert low-grade heat into electrical energy based on the Seebeck effect, demonstrating versatility in emerging wearable electronics for human waste heat collection, soft robotics, health monitoring, and personal thermal management[19–23].

To date, most research on wearable flexible thermoelectric technology focuses primarily on materials, particularly on enhancing thermoelectric performance (measured by the power factor or *ZT*) and improving flexibility and stability[24,25]. Generally, most high-performance thermoelectric materials, especially inorganic ones, are rigid, brittle, and fragile, making it challenging to meet the requirements for flexible wearables[26,27]. Advanced strategies for achieving

[1]Shanghai Frontiers Science Center of Advanced Textiles, College of Textiles, Donghua University, Shanghai, China. [2]School of Chemistry and Physics, ARC Research Hub in Zero-emission Power Generation for Carbon Neutrality and Centre for Materials Science, Queensland University of Technology, Brisbane, QLD, Australia. [3]Center for Civil Aviation Composites, College of Textiles, Donghua University, Shanghai, China. [4]Engineering Research Center of Knitting Technology, Ministry of Education, Jiangnan University, Wuxi, Jiangsu, China. [5]These authors contributed equally: Xinyang He, Xiao-Lei Shi.
✉e-mail: wangliming@dhu.edu.cn; xhqin@dhu.edu.cn; zhigang.chen@qut.edu.au

flexibility, and even elasticity, in TEDs include processing traditional thermoelectric materials into thin films or coating them onto flexible substrates[28–31]. Although the resulting thermoelectric materials can be bent or even stretched, the temperature gradient (ΔT) is typically constructed in the in-plane direction rather than the more ideal out-of-plane (thickness) direction[32]. Moreover, given the inherent challenges in the structural design of flexible, especially wearable TEDs, the progress in this area has been slower than that of thermoelectric materials[33]. To fully harness the potential of thermoelectric materials in devices, it is crucial to optimize the device structure, particularly by enhancing and stabilizing the ΔT across the device while maintaining structural stability and flexibility[4,5]. This remains a significant research challenge. Besides, as discussed above, many researchers focus on improving the thermoelectric performance of materials used in wearable F-TEDs, as higher material performance typically induces greater output power or thermoelectric energy conversion efficiency of devices. However, in some applications that require rapid response, such as powering sensors, only a small device performance is sufficient to drive these sensors. Therefore, under such circumstances, other physical properties of the device, such as response speed, flexibility, wearability, stability, breathability, and washability, become more critical.

Compared to two-dimensional (2D) F-TEDs, three-dimensional (3D) F-TEDs can maximize the collection of body heat, thereby maintaining a sustained out-of-plane ΔT[34]. A common strategy for fabricating 3D F-TEDs involves combining inorganic bulk materials with complex wiring[35]. Although these devices exhibit excellent thermoelectric performance, the bulky and rigid thermoelectric legs greatly compromise comfort and stability during wear[36]. This approach struggles to meet the demands for highly integrated devices, making real-time, synchronized sensing of stimuli such as deformation and temperature challenging. Developing elastic thermoelectric materials is essential for creating 3D TEDs that can adapt in real-time to complex skin changes, comfort needs, multi-channel stimuli, and deformations caused by body movements[37]. The current mainstream strategy involves applying thermoelectric materials to commercial polyurethane foam[38] or mixing them with low-dimensional nanomaterials followed by freeze-drying at low temperatures to create 3D thermoelectric elastomers[39]. However, this non-breathable structure negatively impacts its thermal and moisture exchange properties, and the unstable intrinsic 3D porosity presents challenges to its durability and resilience. Therefore, developing elastic thermoelectric materials and devices that simultaneously offer comfort, high durability, and rapid response remains a significant challenge.

Our work, therefore, focuses on practical usability and is dedicated to designing functional device structures. Here, we report the fabrication and doping modification of highly elastic 3D thermoelectric fabrics using advanced knitting techniques, demonstrating the convenience, controllability, and industrial scalability of elastic thermoelectric textiles. The 3D spacer fabric utilizes 36 dtex spandex filaments with both rigidity and elasticity as spacer yarns to support the intrinsic 3D structure, resulting in the distribution of multiple static air channels within the fabric. This design achieves ultra-low thermal conductivity ($\kappa < 0.05\ W\ m^{-1}\ K^{-1}$), super-fast response time of 20 ms, and stability over more than 10,000 compression cycles. These properties are crucial for maintaining a stable out-of-plane ΔT in TEDs. Unlike bulk/film thermoelectric materials, the spatial structure of the fabric also provides an exceptionally high breathability of 1300 mm s^{-1}, enabling effective heat and moisture exchange between the human body and the external environment. Additionally, the fabric exhibits precise temperature detection with an accuracy of 0.02 K and a rapid temperature response time of 240 ms, ensuring real-time and accurate temperature stimuli transmission. Most importantly, the thermoelectric and piezoresistive effects in the fabric-based device are decoupled, allowing the thermoelectric device to maintain a stable output voltage even under large deformations of up to 50%. The device was sewn into gloves for sign language learning by individuals with speech disabilities. By integrating with our support vector machines (SVM)-based machine learning model, our device achieves 100% prediction accuracy, providing comprehensive and efficient assistance in learning sign language. Equipped with a wireless transmission system, this device can be self-powered worn on various parts of the body to match complex thermal surfaces for monitoring human safety in real-time, such as respiratory diseases and high-temperature alerts, via a mobile app or computer, showing practical application potential.

Results

Device fabrication

We first introduced the design concept behind the thermoelectric spacer fabric (TESF). Figure 1 illustrates the production process and device fabrication schematic of the TESF. Low-cost, high-rigidity 36 dtex polyester monofilament fibers were used as spacer yarns, which were combined with softer 135 dtex and 90 dtex polyester monofilaments through 3D knitting technology for continuous mass production on our machine (Fig. 1a). Warp knitting machines operate without generating direct emissions, carbon emissions, pollutants, or wastewater discharges, thus having a minimal impact on the environment. The loop formation process of the specific double-needle bar warp knitting machine is shown in Supplementary Fig. 1, and detailed knitting procedures are supplemented in the “experimental details” section in the Supplementary Information. The digital diagram of the inlay yarn and its movement are shown in Supplementary Fig. 2. Due to its ease of water processing, non-toxicity, and excellent thermoelectric properties, carbon nanotubes (CNTs) were selected as the thermoelectric fillers for the fabric (Fig. 1b). Oleylamine was used as an n-type dopant for CNTs due to its excellent air stability[40], while poly(3,4-ethylenedioxythiophene):poly(styrene sulfonate) (PEDOT:PSS) and CNT have been reported to exhibit excellent p-type thermoelectric properties[41,42]. Thanks to the cuttability and flexibility of TESF, it can be easily shaped into various forms and labels without leaving marks, making it suitable for integration into everyday wearable devices (Supplementary Fig. 3). As shown in Supplementary Fig. 4, photographs of diverse types of fabrics display that both p-type and n-type thermoelectric fabrics can be woven on a large scale. To understand the doping mechanism of polymers on thermoelectric fabric, we examined the microstructure of the fabrics. The scanning electron microscope (SEM) images of the initial spacer fabric reveal the smooth surface of individual fibers. The interlayer structure between the fabrics is clearly defined, and the gaps between the fibers are distinct (Supplementary Fig. 5). After the introduction of PEDOT:PSS, the individual fibers in the p-type TESF become rough (Supplementary Fig. 6). The characteristic composite layered structure of PEDOT:PSS and CNTs can be observed in the magnified SEM images. In contrast, the surface of the n-type TESF remains smoother, but the oleylamine-doped CNTs wrap, increasing the diameter of the CNT edges (Supplementary Fig. 7). The basic morphology of the fabric shows no significant changes. Although the initial spacer fabrics can be mass-produced using industrialized machines, the preparation of TESF remains challenging. In future work, we plan to integrate an impregnation bath directly at the back end of the knitting process, enabling large-scale and continuous preparation of TESF.

Our TESF is compared to recently reported wearable multifunctional thermoelectric devices in terms of breathability, response speed, accuracy, κ, and durability, and it meets several leading metrics in the field (Fig. 1c)[43–47]. Notably, the permeability of TESF, a crucial factor for wearable devices, reaches 1250 mm s^{-1}. This fully supports heat and moisture exchange during wear, ensuring a comfortable user experience. The ultra-low κ of 0.043 W m^{-1} K^{-1} allows TESF to consistently maintain a stable temperature gradient across the fabric, facilitating accurate temperature signal detection. When compared to

https://doi.org/10.1038/s41467-025-57889-1

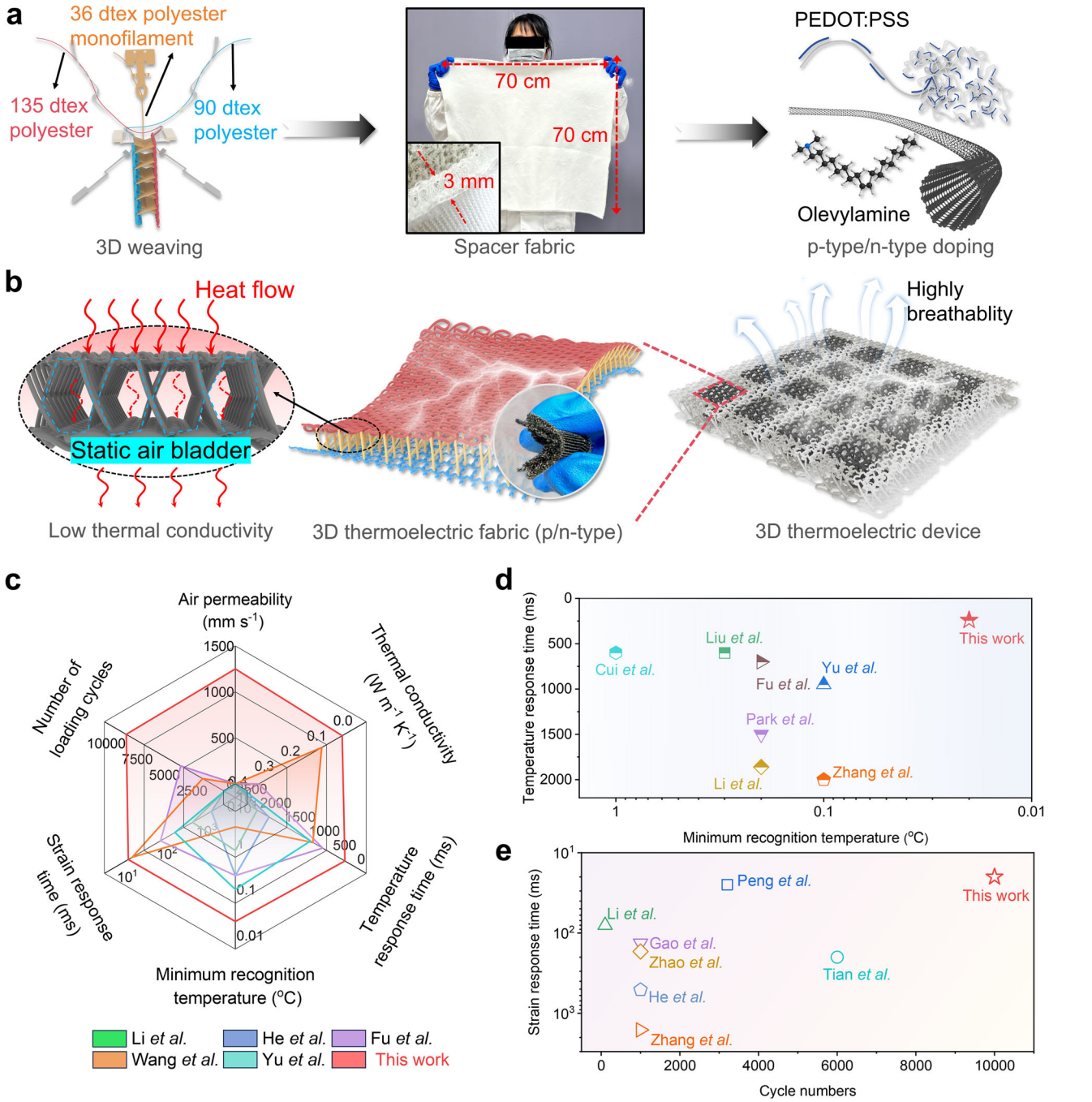

Fig. 1 | Production process and device fabrication schematic of thermoelectric spacer fabric (TESF). a Schematic diagram of bulk spacer fabric preparation. **b** Schematic of three-dimensional (3D) TESF preparation. **c** Comparison of performance metrics of this work with other reported dual-mode thermoelectric materials[43–47]. **d** Comparison of the minimum recognition temperature and temperature response time of this work with other reported studies[21,43,45,47–50]. **e** Comparison of the maximum load cycling and strain response time of this work with other reported studies[44,51–56].

the latest thermoelectric-based temperature sensors, TESF-based sensors exhibit a rapid temperature response of up to 240 ms and precise temperature difference recognition of 0.02 K, both of which represent the high performance levels in available thermoelectric devices (Fig. 1d, see Supplementary Table 1 for detailed comparisons)[21,43,45,47–50]. Additionally, when evaluated against a recently reported 3D thermoelectric compression sensor, our device outperforms in all metrics (Fig. 1e)[44,51–56]. The TESF endures up to 10,000 compression cycles, the maximum reported for thermoelectric devices, and achieves a compression response time of 20 ms, setting a record for response speed in thermoelectric devices (see Supplementary Table 2 for detailed comparisons).

Sensing performance

The 3D structure of the spacer fabric endows the thermoelectric fabric with excellent breathability, which is crucial for heat and moisture exchange during wear (Fig. 2a). The samples were placed on a custom-built electrical testing device to investigate their thermoelectric properties. As shown in Fig. 2b and Supplementary Fig. 8, the original TESF, which contained only CNTs, exhibited a positive Seebeck coefficient (S) of approximately 48.83 μV K^{-1} due to the presence of oxygen impurities, indicating that the charge carriers were holes. After adding PEDOT:PSS as a p-type dopant, the electrical conductivity (σ) and power factor ($S^2\sigma$) increased significantly, consistent with previous studies on CNT/PEDOT:PSS composites[42,57–59]. When oleylamine was

https://doi.org/10.1038/s41467-025-57889-1

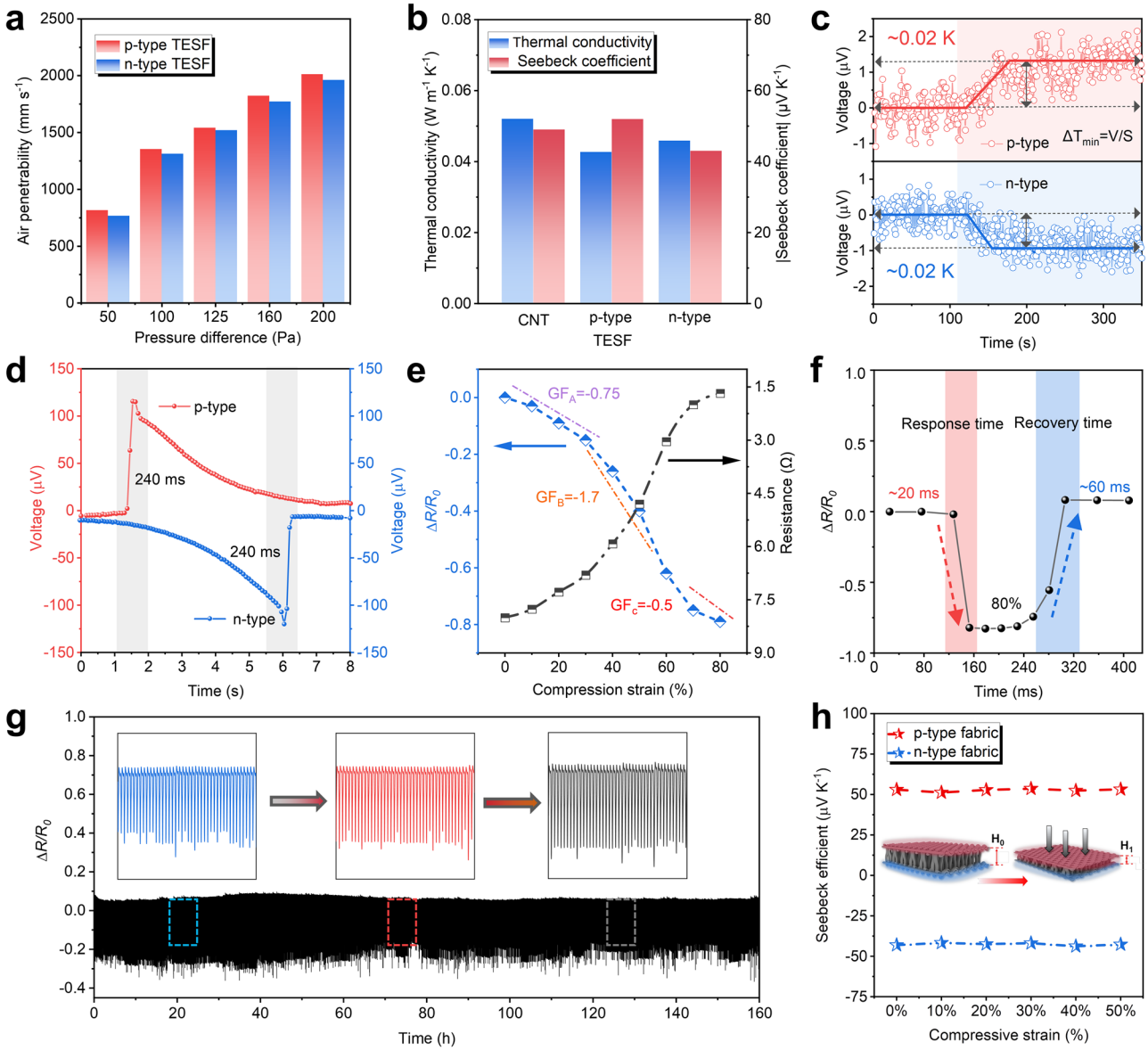

Fig. 2 | Sensing performance testing of TESF. a Air permeability of p-type thermoelectric spacer fabric (TESF) and n-type TESF. All samples were measured three times and averaged. **b** S and thermal conductivity (κ) of carbon nanotubes (CNTs)-based, p-type, and n-type TESF. All samples were measured three times and averaged. **c** Minimum discernible ΔT for p-type and n-type TESF. **d** Temperature sensing response time for p-type and n-type TESF. **e** Resistance response of TESF under different compressive strains, where R is the resistance change value under strain, and R_0 is the initial resistance. **f** Response and recovery speed of TESF under compressive strains. **g** Stability of resistance changes in TESF after 10,000 compressive strain cycles. **h** S of p-type and n-type TESF under different compressive strains.

introduced as an n-type dopant to the CNTs, the S of the fabric switched to a negative value. Additionally, the unique structure of the 3D fabric resulted in a large amount of static air within, allowing TESF to achieve an ultra-low κ superior to other thermoelectric materials with different structural designs. The out-of-plane ΔT makes it easier to maintain a stable output signal when used as a wearable device. The sensitivity of TESF to different temperature differences was first evaluated, and as seen in Supplementary Fig. 9, both p-type and n-type TESF responded sensitively to the respective ΔTs. They were also sensitive to small ΔTs, with the minimum temperature response for p-type/n-type TESF being approximately 0.02 K (Fig. 2c). The response time to temperature changes was just 240 ms (Fig. 2d). Moreover, the output voltages of both n-type and p-type TESF demonstrate remarkable stability under cyclic temperature variations (Supplementary Fig. 10).

Piezoresistivity is an important parameter for evaluating the practical application potential of wearable electronics. The 3D supporting structure of the spacer fabric also lends potential for its use as a piezoresistive sensor. The strong polyester monofilaments in the fabric bend under external pressure and return to their original state once the force is removed (Supplementary Fig. 11a). Supplementary Fig. 11b shows the compression strain-stress curves for different samples. Compared to the initial spacer fabric, the stress in both p-type and n-type TESF significantly increased, due to the rigid effects of the CNTs in the dopants. We selected p-type TESF as a reference to closely examine its mechanical and electrical changes during compression. As shown in Supplementary Fig. 11c, the fabric exhibits no significant hysteresis or fatigue under 10%–50% compression strain, indicating high resistance and recovery (Supplementary Fig. 12).

During dynamic compression and recovery, the spacer yarns in the fabric make contact and separate from the internal surface of the fabric, resulting in a piezoresistive effect. We constructed a 3D compression model, as shown in Supplementary Fig. 13, to reveal the resistance changes during this dynamic process. During compression,

https://doi.org/10.1038/s41467-025-57889-1

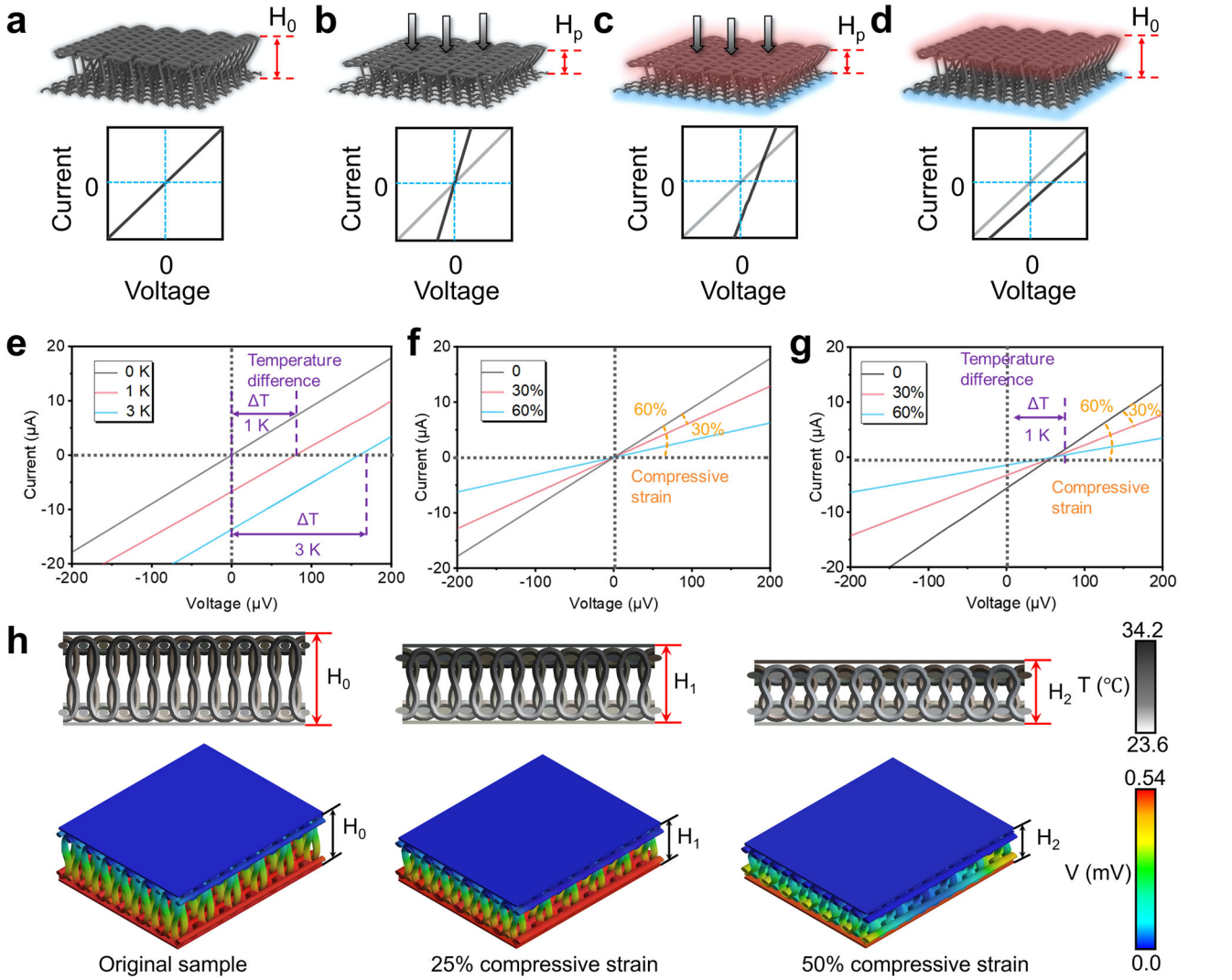

Fig. 3 | Decoupling mechanism of mechanical and thermal stimuli in TESF. *I-V* curves of TESF (**a**) without external stimuli, (**b**) under compressive strain alone, (**c**) under both compressive strain and Δ*T*, (**d**) under Δ*T* only, (**e**) at different Δ*T* values (Δ*T* = 0, 1, and 3 K), (**f**) under various compressive strains (0%, 30%, 60%), and (**g**) under different strains (0%, 30%, 60%) with a constant Δ*T* of 1 K. **h** Finite element simulation of temperature distribution and output thermal voltage of TESF under compressive strain.

the contact angle between the spacer yarns and the two planes decreases, increasing the contact area and creating more conductive pathways. Based on this concept, we evaluated the resistance of the fabrics under different compression deformations to demonstrate their piezoresistive sensing potential (Fig. 2e). The gauge factor (GF) during compression can be categorized into three regimes: A, B, and C. When the compression deformation exceeds 20%, the gauge factor reaches its maximum, approximately 1.7, which corresponds to our previously described equivalent resistance model. Additionally, the response time and recovery time of the fabrics under large deformations are only 20 ms and 60 ms, respectively, fully meeting the real-time requirements for wearable devices (Fig. 2f). Mechanical stability and durability are critical indicators for wearable devices. As shown in Fig. 2g, the piezoresistive signal of the fabric remains stable after 10,000 cycles under a 40% compression strain. Additionally, the resistance and *S* values of both n-type and p-type TESFs remain unchanged after 10,000 compressions, demonstrating that the 3D fabric structure ensures reliable and stable support (Supplementary Fig. 14). Moreover, the thermoelectric properties of both n-type TESF and p-type TESF remain very stable after bending cycles and washing (Supplementary Figs. 15, 16). To investigate the coupling relationship between internal resistance and output voltage during dynamic processes, we evaluated the *S* under different compression strains (Fig. 2h). Remarkably, the *S* of TESF remained unaffected as strain increased. This prompted further investigation into the changes in thermoelectric voltage and thermal resistance under dynamic conditions.

Decoupling mechanism

To explore the decoupling characteristics of TESF, we designed a series of experiments. Taking p-type TESF as an example, we applied independent and coupled stimuli to the fabric and observed changes in the electrical signals. Initially, we measured the *I-V* curve of the fabric in its baseline state (Fig. 3a). When pressure was applied to the fabric, the resistance signal significantly decreased due to the piezoresistive effect, resulting in a noticeable shift in the *I-V* curve (Fig. 3b). Next, while keeping the pressure constant, we applied a Δ*T* to the fabric, which caused the *I-V* curve to shift to the right with the same slope (Fig. 3c). According to the typical thermoelectric mechanism, the output thermoelectric voltage is $S \times \Delta T$. This result indicates that the internal resistance of the fabric is not affected by the inherent temperature variation during the output thermoelectric voltage. Finally,

when the compressive stress was removed, the *I-V* curve returned to a slope parallel to the initial sample, with only a lateral shift in the thermoelectric voltage due to the ΔT (Fig. 3d).

To refine the experimental process, we conducted continuous testing across multiple gradients. As shown in Fig. 3e, the *I-V* curves shift significantly to the right when the fabric is subjected to different ΔTs, indicating clear thermoelectric properties. The *I-V* curves of the fabrics under different compressive strains at a constant temperature difference exhibit varying slopes (Fig. 3f). The slope decreases as the pressure increases, indicating a corresponding reduction in resistance. Notably, the voltage remains unaffected under different pressure conditions. Additionally, we performed compression tests on the fabric under a constant ΔT of 1 K (Fig. 3g). Obviously, applied pressure does not affect the thermoelectric voltage of the fabric; instead, its lateral shift remains consistent with the origin. From these observations, we conclude that the piezoresistive and Seebeck effects of the fabric are fully decoupled. We then connected the fabric to a temperature-variable compression testing facility, as illustrated in Supplementary Fig. 17a, to systematically investigate its decoupling properties under various ΔTs. The ΔT was controlled in real time using a pair of Peltier elements. Initially, we evaluated the internal resistance of the fabric under different compressive strains across a ΔT range of 0 to 30 K (Supplementary Fig. 17b). The results show that the temperature has a minimal effect on resistance, irrespective of the applied compressive strain. Similarly, monitoring the output thermoelectric voltage of the fabric under different compressive strains revealed that pressure has a negligible influence on the thermoelectric voltage (Supplementary Fig. 17c). These findings confirm that in this 3D material, piezoresistive signals and thermoelectric voltage signals change independently of each other. Furthermore, we constructed a 3D equivalent model of the fabric and validated our strategy using finite element analysis. As shown in Fig. 3h, a stable ΔT of 10 K was first applied to the fabric. With the application of compressive strain, the temperature distribution within the fabric remains unaffected, as observed from the contour plot, due to the low κ of the fabric. Since the S remains constant at different compressive strains, the thermoelectric voltage output remains stable. This effectively demonstrates the decoupling characteristics of Seebeck and piezoresistive effects in the 3D fabric.

Irregular deformations caused by human movement significantly impact the output power of the device, and no dedicated work has yet focused on decoupling the signals of this device to enhance its stability. Based on the decoupling characteristics of TESF, we investigated the decoupling performance of integrated devices. The experiments were conducted under conditions with and without thermal sources and pressure, simulating various stimuli coupling caused by temperature transfer and motion during human wear. The device was fabricated by seamlessly integrating eight pairs of p-type and n-type TESF into a 3D fabric substrate (Supplementary Fig. 18). The circuit connections of the device are shown in Supplementary Fig. 19. The entire device measures approximately 5.5 × 5.5 cm, allowing it to be flexibly deformed and making it suitable for everyday wear. As illustrated in Supplementary Fig. 20a, we applied three different conditions to the device: plastic board pressure, palm close, and palm press, using a plastic board and a palm without a thermal source. When pressing the device with a plastic board, the device resistance generates a compressive signal, while the voltage signal remains unchanged (Supplementary Fig. 20b and Supplementary Movie 1). When the palm approaches the device, the resistance signal remains constant. Due to the ΔT caused by the human body and the environment, the device produces a noticeable thermoelectric voltage response (Supplementary Fig. 20c and Supplementary Movie 2). As shown in Supplementary Fig. 20d, when repeatedly pressing the device with the palm, both resistance and voltage signals are output in a decoupled manner due to the piezoresistive and Seebeck effects (Supplementary Movie 3). This indicates that not only TESF, but also the flexible devices fabricated with integrated TESF, exhibit decoupling of resistance signals caused by strain and thermoelectric voltage signals induced by ΔTs.

Sensing applications

We first evaluated the output performance of the device. As shown in Supplementary Fig. 21a, the maximum output power of the device is achieved at different ΔTs when the connected load resistance (R_{load}) is 110 Ω, which matches the internal resistance of the device. This is further validated by the maximum output power at various load resistances, as presented in Supplementary Fig. 21b. For energy harvesting tests, the device was worn on the user's wrist (Supplementary Fig. 21c). An infrared diagram indicates a ΔT of approximately 8 K between the top and bottom of the device, attributed to the low κ of the 3D fabric, which effectively prevents the transfer of body heat to the top surface. Consequently, the device generates a stable and consistent voltage of 5.44 mV (Supplementary Fig. 21d).

The flexibility and high integration of this device make it easy to incorporate into everyday wearable garments. As shown in Fig. 4a, the device was sewn into an N95 mask, creating a wearable smart mask for real-time breath monitoring. According to infrared images, temperature changes at the nose area during inhalation and exhalation cause variations in the ΔT across the device, enabling real-time breath monitoring. When users wear the smart mask, the real-time output thermal voltage distinguishes between facial actions, including normal breathing, coughing, sighing, and deep breathing (Fig. 4b). Importantly, the thermal voltage signal generated by breathing is unaffected by resistance changes caused by airflow vibrations. The accurate recognition of the device allows differentiation and identification of these signals based on the frequency of inhalation and exhalation, the rate of change in the signal, and the peak values of the thermal voltage. For instance, normal breathing shows a slow frequency and low peak values (Fig. 4c). Coughing produces three distinct thermal voltage peaks with a long duration (Fig. 4d). Compared to other actions, signing results in much higher thermal voltage peaks (Fig. 4e). The difference between normal and deep breathing is reflected in the height and frequency of the peaks (Fig. 4f). In addition to assessing breathing conditions, the smart mask can differentiate facial expressions such as smiling, slight smiling, and laughing (Supplementary Fig. 22).

To explore practical applications of the device, we integrated it with a wireless transmission module to build a wearable wireless signal monitoring system. The working principle of the wearable wireless sensing system is shown in Supplementary Fig. 23. Based on the thermoelectric effect, the device generates real-time voltage signals, which are then captured by an analog-to-digital converter and sent to an operational amplifier. The microcontroller collects and analyzes these signals, extracting the waveforms, frequencies, and peak values of the thermoelectric voltage, and transmits the data in real-time to a mobile terminal via Bluetooth. We installed this system into our mask (Supplementary Fig. 24). As shown in Supplementary Fig. 25 and Supplementary Movie 4, when the user breathes normally, the signal sent to the mobile app fluctuates regularly. However, when the user stops breathing, the signal disappears, indicating that the user is in danger and requires immediate assistance. Similarly, we sewed the fabric onto insulating gloves and integrated it with a wireless transmission module to explore temperature warning applications (Supplementary Figs. 26, 27). When the user wears gloves at varying distances from a heat source, the phone collects corresponding signals (Supplementary Fig. 28). As shown in Supplementary Fig. 29 when the gloves are near a flame, a high-temperature threshold is detected; exceeding this threshold poses a burn risk to the user. Therefore, real-

https://doi.org/10.1038/s41467-025-57889-1

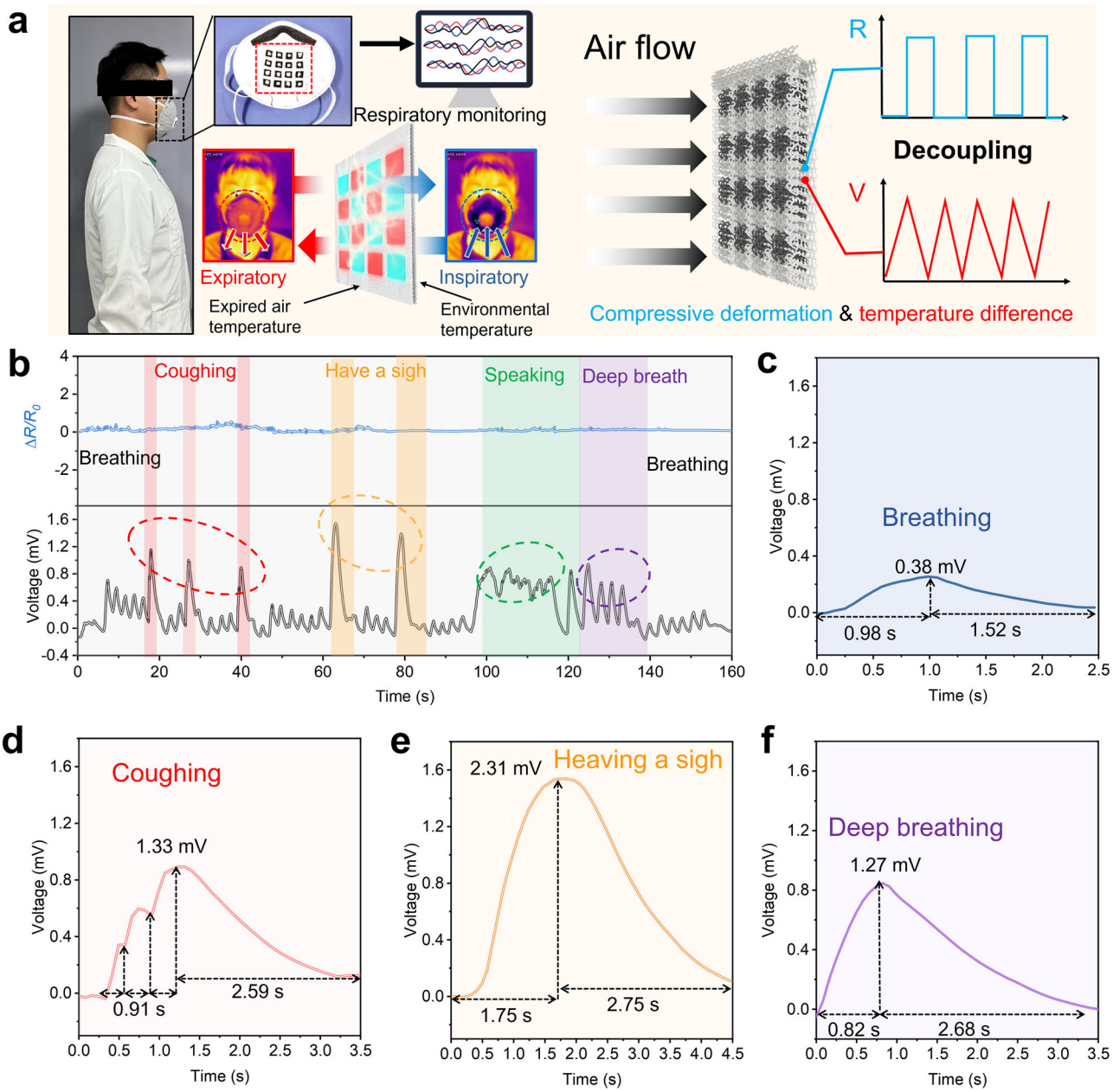

Fig. 4 | Smart mask for respiratory monitoring and disease prediction. **a** Schematic diagram of the smart mask integrated into an N95 mask for monitoring respiratory status, including infrared images showing temperature changes during expiration and inhalation. **b** Real-time thermal voltage output of the smart mask during various respiratory actions, including expiration and inhalation, and magnified views of (**c**) thermal voltage signals during breathing, (**d**) thermal voltage signals during coughing, (**e**) thermal voltage signals during sighing, and (**f**) thermal voltage signals during deep breathing.

time data observed on the phone can provide pre-warning to avoid burns and scalds.

The resistive sensor signals of wearable devices often suffer from temperature-induced interference due to direct contact with the skin, which can reduce the accuracy and scientific validity of the sensing signals. Our TESF, however, can shield against temperature interference in resistance measurements. Therefore, we designed a multifunctional sensor based on TESF (Supplementary Fig. 30). We installed the sensor on the wrist, elbow, and finger joints, and the sensor accurately differentiates various motion amplitudes through the piezoresistive effect (Fig. 5a–c). To monitor the independence of resistance and thermoelectric voltage signals, we also measured the inherent thermoelectric voltage during the sensing tests and found that the thermoelectric voltage is unaffected by motion, which aligns with our conclusions (Supplementary Fig. 31). People with speech impairments require coordinated finger gestures and high interaction for learning sign language. We designed a smart glove capable of converting finger movements into electrical signals, aimed at enhancing sign language learning for individuals with speech impairments (Fig. 5d). We attached a compressive strain sensor to the joints of the glove to capture the pressure generated during finger movements and transmitted the captured signals to a personal computer for performance analysis. Such a smart glove not only addresses the initial challenges of sign language learning for individuals with speech impairments but also provides a method for remote communication for people with disabilities. The output signals of the glove when performing sign language numbers 1-5 are shown in Supplementary Fig. 32.

Additionally, Fig. 5e and Supplementary Fig. 33 display complex sign language gestures, including I LOVE YOU, OK and COOL glove

https://doi.org/10.1038/s41467-025-57889-1

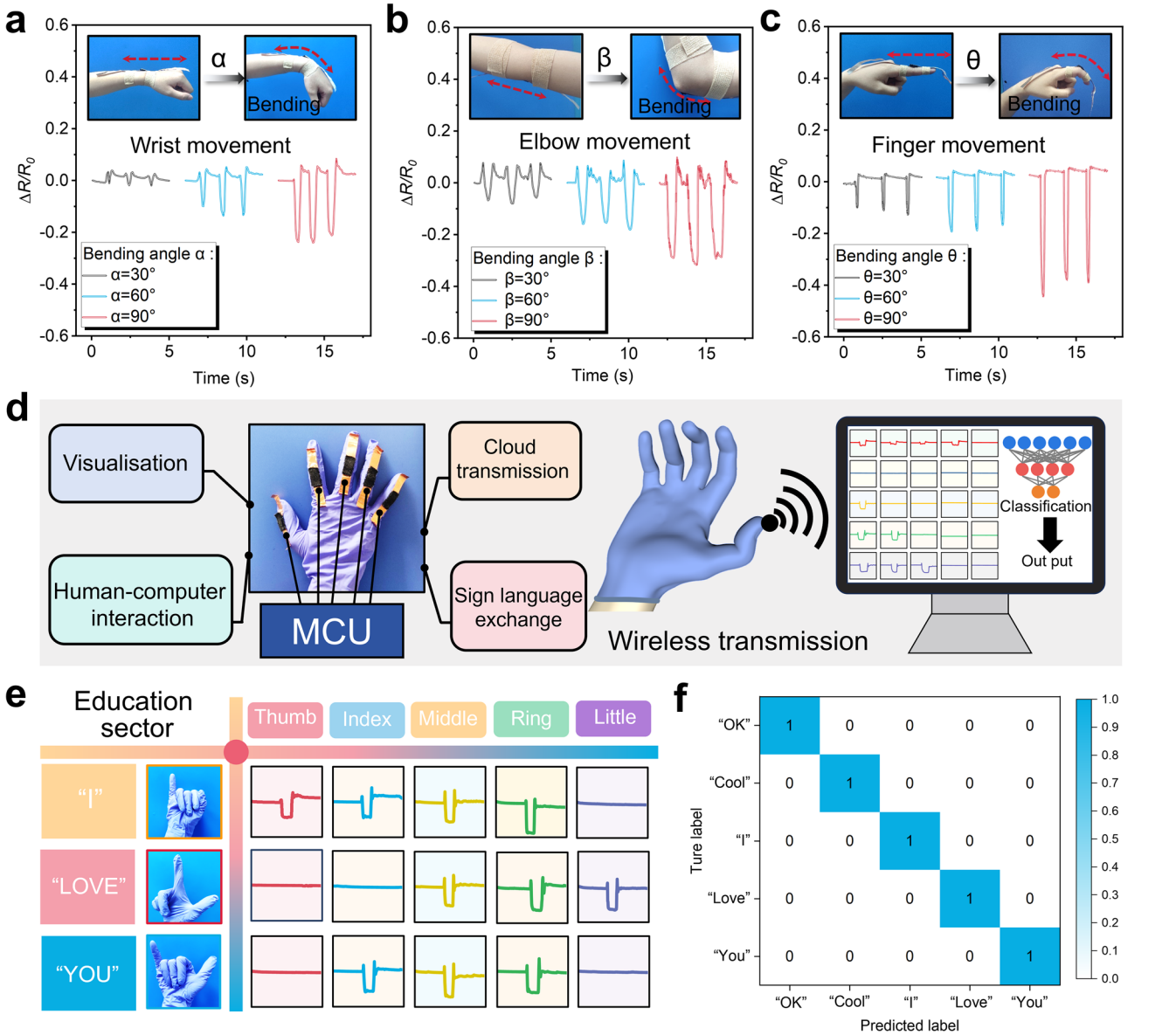

Fig. 5 | TESF pressure sensor-based human-machine interaction applications enhanced by machine learning algorithms. The pressure sensor-based TESF is used to signal bending activity in the (**a**) wrist, (**b**) elbow, and (**c**) finger areas. **d** Schematic of smart glove-assisted sign language training and transformation. **e** Schematic diagram of the corresponding transformation of sign language and sensing signals, where the test signals are all $\Delta R/R_O$. **f** Confusion matrix of gesture recognition with an accuracy of 100%.

signals. By distinguishing the arrangement and combination of finger movements, specific meanings can be assigned. The collected signals of the smart glove can be interpreted to understand sign language by analyzing these finger movement patterns. To achieve intelligent recognition of sign language gestures, we designed and implemented a machine learning model based on SVM for precise classification and recognition of complex device signals and developed a machine learning-assisted sign language training strategy (Supplementary Fig. 34). In the implementation process, we first extracted key attributes of the signals through feature engineering and then used a radial basis function (RBF) kernel to enhance the non-linear classification capabilities of SVM. Additionally, we optimized the hyperparameters of the model using grid search and cross-validation strategies, which significantly improved the classification accuracy. The model can achieve a 100% classification accuracy across multiple independent test datasets (Fig. 5f and Supplementary Fig. 35).

Discussion

In this work, we report an advanced strategy for the scalable fabrication of highly elastic 3D thermoelectric fabrics. A combined weaving approach has been used to construct a 3D structure with excellent support characteristics, resulting in multiple static air channels distributed within the fabric, which endows an ultra-low κ, super-high breathability, and stability. Such a character ensures continuity of the through-thickness temperature gradient and durability during use. Additionally, the fabric achieves precise temperature resolution and exhibits compression hysteresis, ensuring real-time, accurate response to sensory stimuli. Due to its inherent multiple static air distribution, the 3D device maintains stable output signals even under 50% compression deformation. Wearable devices made from this fabric can be integrated with Bluetooth modules for real-time, accurate monitoring of signals from various body locations. This has significant implications for early warning of respiratory diseases and early detection of thermal hazards to users. Furthermore, by incorporating the proposed SVM-

based machine learning model, we developed smart gloves that assist individuals with disabilities in learning sign language, achieving a sign language recognition accuracy of 100%. Thus, the devices we develop have broad practical application potential.

Methods

Materials

CNT dispersion (1–2 nm in diameter, TNWDS, dispersed in water) was sourced from Chengdu Organic Chemicals Co., Ltd., Chinese Academy of Sciences. Dimethyl sulfoxide (DMSO) was obtained from Sigma-Aldrich Shanghai Trading Co., Ltd., and absolute ethanol (99.5%) was purchased from Sinopharm Chemical Reagent Co., Ltd. Poly(3,4-ethylenedioxythiophene):poly(styrene sulfonate) (PEDOT:PSS, 1.3 wt% dispersion in H_2O, conductive grade) was also acquired from Sigma-Aldrich Shanghai Trading Co., Ltd. Oleylamine was purchased from Shanghai Aladdin Biochemical Technology Co., Ltd. Polyester fully drawn yarn (FDY) and polyester monofilament were provided as well. All chemicals and materials were used as received without further purification.

Preparation of warp-knitted spacer fabric

Typically, warp-knitted spacer fabrics are composed of interwoven polyester filaments, with one side forming a hexagonal mesh structure and the other a flat, structured fabric. The hexagonal mesh side consists of a warp knit and satin weave, while the flat structured layer is a tricot knit. The loop diagram and yarn threading for these structures are illustrated in Supplementary Fig. 1 and Fig. 2.

Preparation of CNT thermoelectric spacer fabric (TESF) and p/n-type TESF

In a typical process, the 50 mL CNT dispersion was first mixed with deionized water at a 1:2 ratio using a cell crusher. The spacer fabrics were then fully immersed in this mixture and dried at 80 °C. The CNT TESF was obtained by washing the fabrics three times each with deionized water and alcohol, followed by drying. TESF is prepared using water as a solvent, ensuring no contamination from organic solvents. PEDOT: PSS was mixed with water at a 1:1 ratio and stirred for 1 hour at room temperature. The homogeneously mixed dispersion was then slowly added dropwise to the CNT-TESF and dried at 80 °C to produce the p-type TESF. DMSO was subsequently added dropwise to the resulting fabric, which was maintained at 80 °C for 5 minutes. Finally, the p-type TESF was obtained by washing it twice with deionized water. 5 ml of oleylamine was mixed with 40 ml of ethanol with vigorous stirring for three hours. The homogeneously mixed solution obtained was slowly added dropwise to the CNT TESF and dried at 40 °C to obtain the n-type TESF. The preparation process involves solely solution impregnation without any chemical reactions or synthesis, making it environmentally friendly.

Characterization

The surface and cross-sectional morphology of the fabrics, as well as the distribution of CNTs, were characterized using field-emission scanning electron microscopy (FE-SEM, Hitachi SU-8010). The compression strain properties of the fabrics were evaluated using a universal material testing machine (CTM2050 Microcomputer Control Electronic Universal Testing Machine, Xie Qiang Instrument Manufacturing, Shanghai, China). The air permeability of the samples was measured using a fully automatic air permeability tester (YG461E). Thermographic imaging of the samples was performed with an infrared camera (Fotric 226, China). Parameters related to the S and self-powered temperature sensing were obtained using a custom-made setup. In this process, CNT/p-type/n-type TESF samples with dimensions of 1×1 cm and 1×3 cm were prepared, with cold and hot sources applied to their upper and lower ends for precise measurement. Temperature control was managed via commercially available Peltier elements connected to a DC power supply (KEYSIGHT, E3634A). The output voltage was recorded and exported via a multimeter (Keithley 2450). S data were calculated by fitting the data obtained from multimeter measurements, and the sensing signals of the device were recorded in real-time using the same multimeter. The temperature difference of the minimum temperature difference test species is measured as follows: copper wires are connected to both sides of the TESF, silver paste is used to reduce the contact resistance, and the spacing between the two electrodes is D. Two T-type thermocouples are affixed to the left and right sides of the TESF, with a spacing in the middle of the spacing of L. The difference in temperature between the two thermocouples is measured as ΔT_c, and therefore the temperature difference between the electrodes is $\Delta T = \Delta T_c \times D/L$. The temperature difference between the electrodes is measured by the temperature difference between the electrodes is $\Delta T = \Delta T_c \times D/L$.

Data availability

The data generated in this study are provided in the Source Data file. All data are available from the corresponding author upon request. Source data are provided with this paper.

References

1. Yang, Q. et al. Flexible thermoelectrics based on ductile semiconductors. *Science* **377**, 854–858 (2022).
2. Zhao, P. et al. Plasticity in single-crystalline Mg_3Bi_2 thermoelectric material. *Nature* **631**, 777–782 (2024).
3. Wang, D. et al. Multi-heterojunctioned plastics with high thermoelectric figure of merit. *Nature* **632**, 528–535 (2024).
4. Shi, X.-L. et al. Advancing flexible thermoelectrics for integrated electronics. *Chem. Soc. Rev.* **53**, 9254–9305 (2024).
5. Chen, W. et al. Nanobinders Advance Screen-Printed Flexible Thermoelectrics. *Science* **386**, 1265–1271 (2024).
6. Zhao, L.-D. et al. Ultrahigh power factor and thermoelectric performance in hole-doped single-crystal SnSe. *Science* **351**, 141–144 (2016).
7. Ibáñez, M. et al. High-performance thermoelectric nanocomposites from nanocrystal building blocks. *Nat. Commun.* **7**, 10766 (2016).
8. Ortega, S. et al. Bottom-up engineering of thermoelectric nanomaterials and devices from solution-processed nanoparticle building blocks. *Chem. Soc. Rev.* **46**, 3510–3528 (2017).
9. Hou, C. & Zhu, M. Semiconductors flex thermoelectric power. *Science* **377**, 815–816 (2022).
10. Lu, Y. et al. Staggered-layer-boosted flexible Bi_2Te_3 films with high thermoelectric performance. *Nat. Nanotechnol.* **18**, 1281–1288 (2023).
11. Jin, Q. et al. Flexible layer-structured Bi_2Te_3 thermoelectric on a carbon nanotube scaffold. *Nat. Mater.* **18**, 62–68 (2019).
12. Ding, Y. et al. High Performance n-Type Ag_2Se Film on Nylon Membrane for Flexible Thermoelectric Power Generator. *Nat. Commun.* **10**, 841 (2019).
13. Wang, L. et al. Exceptional thermoelectric properties of flexible organic-inorganic hybrids with monodispersed and periodic nanophase. *Nat. Commun.* **9**, 3817 (2018).
14. Yang, G. et al. The role of spin in thermoelectricity. *Nat. Rev. Phys.* **5**, 466–482 (2023).
15. Wang, X., Du, Y., Dou, S. & Zhang, C. Room Temperature Giant and Linear Magnetoresistance in Topological Insulator Bi_2Te_3 Nanosheets. *Phys. Rev. Lett.* **108**, 266806 (2012).
16. Yang, G. et al. Ultra-High Thermoelectric Performance in Bulk BiSbTe/Amorphous Boron Composites with Nano-Defect Architectures. *Adv. Energy Mater.* **10**, 2000757 (2020).

17. Zhao, L. et al. Significant enhancement of figure-of-merit in carbon-reinforced Cu_2Se nanocrystalline solids. *Nano Energy* **41**, 164–171 (2017).
18. Wang, Y. et al. Advancements in Nanotechnology-Based PEDOT and Its Composites for Wearable Thermoelectric Applications. *Small Sci.* **4**, 2400149 (2024).
19. Mao, J. et al. High thermoelectric cooling performance of n-type Mg_3Bi_2-based materials. *Science* **365**, 495–498 (2019).
20. Liu, Y. et al. Scalable-produced 3D elastic thermoelectric network for body heat harvesting. *Nat. Commun.* **14**, 3058 (2023).
21. Zhang, F., Zang, Y., Huang, D., Di, C.-A. & Zhu, D. Flexible and self-powered temperature–pressure dual-parameter sensors using microstructure-frame-supported organic thermoelectric materials. *Nat. Commun.* **6**, 8356 (2015).
22. Mao, J., Chen, G. & Ren, Z. Thermoelectric cooling materials. *Nat. Mater.* **20**, 454–461 (2021).
23. Fiedler, C., Calcabrini, M., Liu, Y. & Ibáñez, M. Unveiling Crucial Chemical Processing Parameters Influencing the Performance of Solution-Processed Inorganic Thermoelectric Materials. *Angew. Chem. Int Ed.* **63**, e202402628 (2024).
24. Yang, D. et al. Flexible power generators by Ag_2Se thin films with record-high thermoelectric performance. *Nat. Commun.* **15**, 923 (2024).
25. Kang, M. et al. Self-Powered Temperature Electronic Skin Based on Island-Bridge Structure and Bi-Te Micro-Thermoelectric Generator for Distributed Mini-Region Sensing. *Adv. Mater.* **35**, 2309629 (2023).
26. He, W. et al. High thermoelectric performance in low-cost $SnS_{0.91}Se_{0.09}$ crystals. *Science* **365**, 1418–1424 (2019).
27. Chang, C. et al. 3D charge and 2D phonon transports leading to high out-of-plane *ZT* in n-type SnSe crystals. *Science* **360**, 778–783 (2018).
28. Zheng, Z.-H. et al. Harvesting waste heat with flexible Bi_2Te_3 thermoelectric thin film. *Nat. Sustain* **6**, 180–191 (2023).
29. Wang, L. et al. Solution-Printable Fullerene/TiS_2 Organic/Inorganic Hybrids for High-Performance Flexible *n*-Type Thermoelectrics. *Energy Environ. Sci.* **11**, 1307–1317 (2018).
30. Nan, K. et al. Compliant and stretchable thermoelectric coils for energy harvesting in miniature flexible devices. *Sci. Adv.* **4**, eaau5849 (2018).
31. Hao, Y. et al. Stretchable Thermoelectrics: Strategies, Performances, and Applications. *Adv. Funct. Mater.* **32**, 2109790 (2022).
32. Sun, T. et al. Stretchable Fabric Generates Electric Power from Woven Thermoelectric Fibers. *Nat. Commun.* **11**, 572 (2020).
33. Shi, X.-L. et al. Advances in flexible inorganic thermoelectrics. *EcoEnergy* **1**, 296–343 (2023).
34. Xia, B. et al. Vertically designed high-performance and flexible thermoelectric generator based on optimized PEDOT:PSS/SWCNTs composite films. *Chem. Eng. J.* **486**, 150305 (2024).
35. Bao, X. et al. Mechanical properties of thermoelectric generators. *J. Mater. Sci. Technol.* **148**, 64–74 (2023).
36. Balazs, D. M. & Ibáñez, M. Widening the use of 3D printing. *Science* **381**, 1413–1414 (2023).
37. Deng, Y.-Y. et al. High-performance thermoelectric PEDOT:PSS fiber bundles *via* rational ionic liquid treatment. *Chem. Eng. J.* **502**, 158104 (2024).
38. Mano, G. et al. Fabrication, characterization, and thermoelectric properties of soft polyurethane foam loaded with semiconducting poly(3-hexylthiophene) nanofibers. *J. Appl Polym. Sci.* **139**, 52354 (2022).
39. Zhang, L. et al. Fiber-Based Thermoelectric Generators: Materials, Device Structures, Fabrication, Characterization, and Applications. *Adv. Energy Mater.* **8**, 1700524 (2018).
40. Sun, T. et al. Wavy-structured thermoelectric device integrated with high-performance n-type carbon nanotube fiber prepared by multistep treatment for energy harvesting. *Compos Commun.* **27**, 100871 (2021).
41. Jabri, M., Masoumi, S., Kandukuri, T. R. & Occhipinti, L. G. Flexible thin-film thermoelectric generators for human skin-heat harvesting: A numerical study. *Nano Energy* **129**, 110001 (2024).
42. Kim, D., Kim, Y., Choi, K., Grunlan, J. C. & Yu, C. Improved Thermoelectric Behavior of Nanotube-Filled Polymer Composites with Poly(3,4-ethylenedioxythiophene) Poly(styrenesulfonate). *ACS Nano* **4**, 513–523 (2010).
43. Fu, Y. et al. Ultraflexible Temperature-Strain Dual-Sensor Based on Chalcogenide Glass-Polymer Film for Human-Machine Interaction. *Adv. Mater.* **36**, 2313101 (2024).
44. He, Y., Lin, X., Feng, Y., Luo, B. & Liu, M. Carbon Nanotube Ink Dispersed by Chitin Nanocrystals for Thermoelectric Converter for Self-Powering Multifunctional Wearable Electronics. *Adv. Sci.* **9**, 2204675 (2022).
45. Li, F. et al. Printable and Stretchable Temperature-Strain Dual-Sensing Nanocomposite with High Sensitivity and Perfect Stimulus Discriminability. *Nano Lett.* **20**, 6176–6184 (2020).
46. Wang, Y. et al. Self-powered wearable pressure sensing system for continuous healthcare monitoring enabled by flexible thin-film thermoelectric generator. *Nano Energy* **73**, 104773 (2020).
47. Yu, H. et al. Flexible temperature-pressure dual sensor based on 3D spiral thermoelectric Bi_2Te_3 films. *Nat. Commun.* **15**, 2521 (2024).
48. Cui, Y. et al. Highly Stretchable, Sensitive, and Multifunctional Thermoelectric Fabric for Synergistic-Sensing Systems of Human Signal Monitoring. *Adv. Fiber Mater.* **6**, 170–180 (2024).
49. Liu, S., Zhang, M., Kong, J., Li, H. & He, C. Flexible, durable, green thermoelectric composite fabrics for textile-based wearable energy harvesting and self-powered sensing. *Compos Sci. Technol.* **243**, 110245 (2023).
50. Park, H. et al. Microporous Polypyrrole-Coated Graphene Foam for High-Performance Multifunctional Sensors and Flexible Supercapacitors. *Adv. Funct. Mater.* **28**, 1707013 (2018).
51. Zhang, D., Zhang, K., Wang, Y., Wang, Y. & Yang, Y. Thermoelectric effect induced electricity in stretchable graphene-polymer nanocomposites for ultrasensitive self-powered strain sensor system. *Nano Energy* **56**, 25–32 (2019).
52. Tian, Y. et al. Ultra-stretchable, sensitive and breathable electronic skin based on TPU electrospinning fibrous membrane with microcrack structure for human motion monitoring and self-powered application. *Chem. Eng. J.* **480**, 147899 (2024).
53. Zhao, X. et al. Thermoelectric generator based on anisotropic wood aerogel for low-grade heat energy harvesting. *J. Mater. Sci. Technol.* **120**, 150–158 (2022).
54. Gao, X.-Z. et al. Self-Powered Resilient Porous Sensors with Thermoelectric Poly(3,4-ethylenedioxythiophene):Poly(styrenesulfonate) and Carbon Nanotubes for Sensitive Temperature and Pressure Dual-Mode Sensing. *ACS Appl Mater. Interfaces* **14**, 43783–43791 (2022).
55. Li, M. et al. Large-Area, Wearable, Self-Powered Pressure–Temperature Sensor Based on 3D Thermoelectric Spacer Fabric. *ACS Sens* **5**, 2545–2554 (2020).
56. Peng, J. et al. MXene-based thermoelectric fabric integrated with temperature and strain sensing for health monitoring. *J. Mater. Sci. Technol.* **212**, 272–280 (2025).
57. He, X. et al. Continuous manufacture of stretchable and integratable thermoelectric nanofiber yarn for human body energy harvesting and self-powered motion detection. *Chem. Eng. J.* **450**, 137937 (2022).
58. Kim, J.-Y., Lee, W., Kang, Y. H., Cho, S. Y. & Jang, K.-S. Wet-Spinning and Post-Treatment of CNT/PEDOT:PSS Composites for Use in

Organic Fiber-Based Thermoelectric Generators. *Carbon* **133**, 293–299 (2018).
59. Hsu, J.-H. & Yu, C. Sorting-free utilization of semiconducting carbon nanotubes for large thermoelectric responses. *Nano Energy* **67**, 104282 (2020).

Acknowledgements

This work was partly supported by the Fundamental Research Funds for the Central Universities (2232023A-05), the grants (52373069 and 52373032) from the National Natural Science Foundation of China. ZGC thanks the financial support from the Australian Research Council and the QUT Capacity Building Professor Program. This work was enabled using the Central Analytical Research Facility hosted by the Institute for Future Environments at QUT.

Author contributions

Z.-G.C., X.H.Q. and L.M.W. supervised the project and conceived the idea. X.Y. H. and X.-L.S. designed the experiments and wrote the manuscript. X.Y.H., X.Y.W., C.Z.L., W.-D.L., H.H.Z., and X.L.Y. performed the sample preparation, structural characterization, and thermoelectric property measurements. W.-D.L., C.Z.L. and H.H.Z. conduct the finite element simulations. X.Y.H., X.-L.S., L.M.W., and Z.-G.C. analyzed the data. All the authors discussed the results and commented on the manuscript. All authors have approved the final version of the manuscript.

Competing interests

The authors declare no competing interests.

Additional information

Supplementary information The online version contains supplementary material available at https://doi.org/10.1038/s41467-025-57889-1.

Correspondence and requests for materials should be addressed to Liming Wang, Xiaohong Qin or Zhi-Gang Chen.

Peer review information *Nature Communications* thanks the anonymous reviewer(s) for their contribution to the peer review of this work. A peer review file is available.

Reprints and permissions information is available at http://www.nature.com/reprints

Publisher's note Springer Nature remains neutral with regard to jurisdictional claims in published maps and institutional affiliations.

Open Access This article is licensed under a Creative Commons Attribution-NonCommercial-NoDerivatives 4.0 International License, which permits any non-commercial use, sharing, distribution and reproduction in any medium or format, as long as you give appropriate credit to the original author(s) and the source, provide a link to the Creative Commons licence, and indicate if you modified the licensed material. You do not have permission under this licence to share adapted material derived from this article or parts of it. The images or other third party material in this article are included in the article's Creative Commons licence, unless indicated otherwise in a credit line to the material. If material is not included in the article's Creative Commons licence and your intended use is not permitted by statutory regulation or exceeds the permitted use, you will need to obtain permission directly from the copyright holder. To view a copy of this licence, visit http://creativecommons.org/licenses/by-nc-nd/4.0/.

© The Author(s) 2025